

Mechanisms of Dual-Band Emission in Sb-Doped Rare-Earth Phosphates Revealed

Ruijie Hao,^{1,2,3} Xin Zhao,^{1,2,3} and Chang-Kui Duan^{1,2,3,4,*}

¹*CAS Key Laboratory of Microscale Magnetic Resonance, and School of Physical Sciences, University of Science and Technology of China, Hefei 230026, China*

²*Anhui Province Key Laboratory of Scientific Instrument Development and Application, University of Science and Technology of China, Hefei 230026, China*

³*CAS Center for Excellence in Quantum Information and Quantum Physics, University of Science and Technology of China, Hefei 230026, China*

⁴*Hefei National Laboratory, University of Science and Technology of China, Hefei 230088, China*

The Sb^{3+} ion has garnered significant interest due to its effectiveness in boosting the optical properties of host materials. Among the interesting phenomena is the commonly observed dual-band emission, which has often been interpreted by adopting the phenomenological model that explains the dual-band emission (“ultraviolet band” and “visible band”) in Sb-doped LPO_4 ($L = \text{Sc}, \text{Y}, \text{Lu}$). However, the model for Sb-doped LPO_4 series itself has not been well understood theoretically. In this work, we employ first-principles calculations combined with group-theory analysis to clarify the underlying physical mechanism behind dual-band emission in Sb-doped LPO_4 series. We demonstrate that the dual-band arises from two excited-state equilibrium structures, one exhibits a relatively small distortion with respect to the ground-state equilibrium structure, while the other displays a significantly larger distortion, characteristic of an “off-center” configuration. The deviations from the ground-state configuration are dominated by two distinct vibrational modes, b_2 and e modes, involving the Jahn-Teller effect and the pseudo Jahn-Teller effect, respectively. Furthermore, charge transition levels and energy barriers calculated using the climbing image nudged elastic band (CI-NEB) method have aided in understanding the relaxation between the two excited-state configurations and the property changes across the Sc, Y, and Lu series. These insights provide a basis for understanding the exotic properties of Sb^{3+} in other hosts and may facilitate the design of optical materials in a broader range of systems involving Sb^{3+} ions.

I. INTRODUCTION

Sb^{3+} ions have recently garnered widespread attention due to their ability to passivate deep-level defects and enhance carrier mobility within the perovskite layer [1, 2], broadband emission, anti-thermal quenching, and tunable luminescence properties [3, 4]. By tuning the coordination environment of the doping centers and altering the type of monovalent cations, a broad spectrum of fluorescence colors can be achieved, ranging from blue to near-infrared [4–8].

Recently, it has been widely recognized that Sb dopants can produce not only single-band [4, 9–14] but also dual-band [15–24] emissions, in addition to the host luminescence. For example, in the case of isovalent substitution, Sb^{3+} : $\text{Cs}_2\text{NaInCl}_6$ [4, 12], $\text{Cs}_2\text{NaYCl}_6$ [14], and Rb_3InCl_6 [11] exhibit single-band emission. In contrast, in the case of aliovalent substitution, Sb^{3+} : $\text{Cs}_2(\text{Sn}, \text{Zr}, \text{Hf})\text{Cl}_6$ [15–17] and RbCdCl_3 , CsCdCl_3 [18–20] display dual-band emission. The interpretation of the mechanism behind dual-band emission goes beyond the phenomenological model of isolated ions and includes the following two regimes:

- (i) Different local minima of the adiabatic potential energy surface (APES) of the excited states [25]

- (ii) Distinct luminescent centers, with variations in diverse site occupations and the influence of neighboring point defects accompanying the dopant.

The first regime often involves the coupling of orbitally degenerate excited states with degenerate vibrational modes at a high-symmetry site, belonging to the Jahn-Teller effect. The second regime often involves either different potential sites in the lattice for occupation, or non-equivalent charges between dopants and the replaced host ions. The presence or absence of an intrinsic defect near the dopant notably affects the material’s optical properties. In practice, due to the broad-band nature of the emissions, not all emissions can be resolved, and some sites or local minima may not produce emissions due to quenching. This often allows different phenomenological interpretations of experimental phenomena, thereby posing challenges in determining the true luminescence mechanisms.

More recently, we studied several systems where Sb^{3+} substitutes host ions with higher [26, 27] or a lower valence state [28], and discovered that intrinsic defects have multiple impacts on aliovalent doping centers. These include the formation of multiple luminescent centers [26–29] and the stabilization of two or more excited-state equilibrium configurations [28].

Actually, Sb^{3+} -related dual-band emission has been reported for a long time in LPO_4 ($L = \text{Sc}, \text{Y}, \text{Lu}$) systems [30, 31]. The intensity ratio of the “UV band” (ultraviolet) to the “visible band” varies non-monotonically with temperature. This phenomenon is particularly in-

* ckduan@ustc.edu.cn

triguing because it lacks the high orbital-degeneracy similar to that described in [25]. Additionally, it does not involve aliovalent doping centers, as Sb^{3+} substitutes a single L^{3+} site with D_{2d} point-group symmetry, maintaining the same valence state. Phenomenologically, G. Blasse and co-workers [30, 31] still attributed the dual-band emission of Sb^{3+} in the $L\text{PO}_4$ to a sort of Jahn-Teller effect. This phenomenological model has been applied [21–24] to interpret various observed dual-band emission. However, there is still a lack of details in the mechanism and no reliable first-principles calculations to confirm the interpretation of the experimental phenomena.

In this work, we combine group-theoretical analysis of electron-vibration mode coupling with first-principles calculations based on (hybrid) density functional theory to obtain the excited state equilibrium structural characteristics and APES of Sb^{3+} -doped rare-earth phosphates. At the D_{2d} ground state equilibrium structure, the three-fold degenerate orbital part of the spin-triplet excited state of isolated Sb^{3+} dopant splits into a non-degenerate B_2 level and a doubly-degenerate E level. Depending on the dominance of different electron-vibration couplings, two distinct mechanisms can lead to structural distortions in the excited states. The first mechanism primarily involves linear coupling within the degenerate E level with non-degenerate vibrational modes. This coupling results in distorted equilibrium configurations along the non-degenerate vibration modes and lifts the degeneracy of the excited level, known as the JT effect. The second mechanism primarily involves coupling between the E level and the non-degenerate B_2 level via the e vibrational mode. Additionally, there is second-order coupling within the E level by the e -vibration mode, leading to different distorted equilibrium configurations in the plane of the doubly-degenerate e mode, which also lifts the degeneracy, known as the pseudo-JT effect) [32, 33]. These two mechanisms are shown to be responsible for the observed “UV band” and “visible band.”

This study provides a in-depth understanding of the dual-band emission of Sb^{3+} -doped materials. It also shows that under certain conditions, the interplay of ligand fields, lattice vibrations, and spin-orbit interactions may lead to rich phenomena in excited state dynamics.

II. METHODOLOGY

A. Lattice optimization

The first-principles calculations were carried out with the projector augmented wave method (PAW) [34] implemented in the Vienna ab initio simulation package (VASP) code [35, 36]. The primitive cell of $L\text{PO}_4$ ($L = \text{Sc}, \text{Y}, \text{Lu}$) were optimized with the Perdew-Burke-Ernzerhof revised for solids (PBEsol) [37] exchange correlation functional under the 520 eV cutoff energy. The k -grids generated by the VASPKIT [38] were set as $7 \times$

7×7 . For comparison, we employed the PBE027 hybrid functional to optimize the lattice constants of $L\text{PO}_4$, with a plane-wave cutoff energy set to 520 eV. The exchange fraction α was consistent with our previous studies [39], adopting $\alpha = 0.27$ for three hosts, labeled as PBE027. To reduce computational cost, a $3 \times 3 \times 3$ k -grids were utilized. The calculated results are summarized in Table I. We observed that the lattice parameters obtained using the PBEsol functional agree better with experimental values, whereas the PBE027 functional tends to systematically underestimate them. Consequently, we adopted the PBEsol-calculated lattice parameters for all subsequent calculations.

TABLE I. The lattice constants (in units of Å) of the tetragonal zircon structure $L\text{PO}_4$ ($L = \text{Sc}, \text{Y}, \text{Lu}$) conventional cell optimized by PBEsol and PBE027. Relative error of lattice parameter (Δ) given with respect to experimental values. Considering the computational cost, k -grids of PBE027 were set as $3 \times 3 \times 3$.

	PBEsol	Δ	PBE027	Δ	Exp. [40]
ScPO_4	a 6.583	0.14%	6.531	−0.65%	6.574
	c 5.786	−0.08%	5.754	−0.64%	5.791
YPO_4	a 6.8820	0.004%	6.839	−0.62%	6.8817
	c 6.0111	−0.11%	5.973	−0.74%	6.0177
LuPO_4	a 6.744	−0.71%	6.698	−1.38%	6.792
	c 5.903	−0.86%	5.869	−1.43%	5.954

B. Electronic structure

The k paths in the Brillouin zone, going between the high-symmetry k points for the band structure calculations, were generated via the SeeK-path package [41]. Electronic band structures of the optimized unit cell by PBEsol were calculated using the PBEsol functional and the PBE027 hybrid functional. A more rigorous approach to compute the accurate bandgap was applying many body perturbation theory within the GW_0 approximation [42]. We performed partially self-consistent quasi-particle GW_0 calculations [43], using the GGA PBEsol functional as the starting point for the GW_0 approach. The details of the parameters used in the GW_0 calculation are presented in the Supplemental Material [44].

C. Excited-state calculations

Supercells with new base vectors ($\mathbf{a}-\mathbf{b}, \mathbf{a}+\mathbf{b}, 2\mathbf{c}$) containing 96 atoms and the Γ -point only in the Brillouin zone were employed to study the defect-related properties. The Sb atom replaces an L atom at a site closest to the center of the supercell. The energy cutoff was set to 520 eV, and the single Γ -point was applied to sample

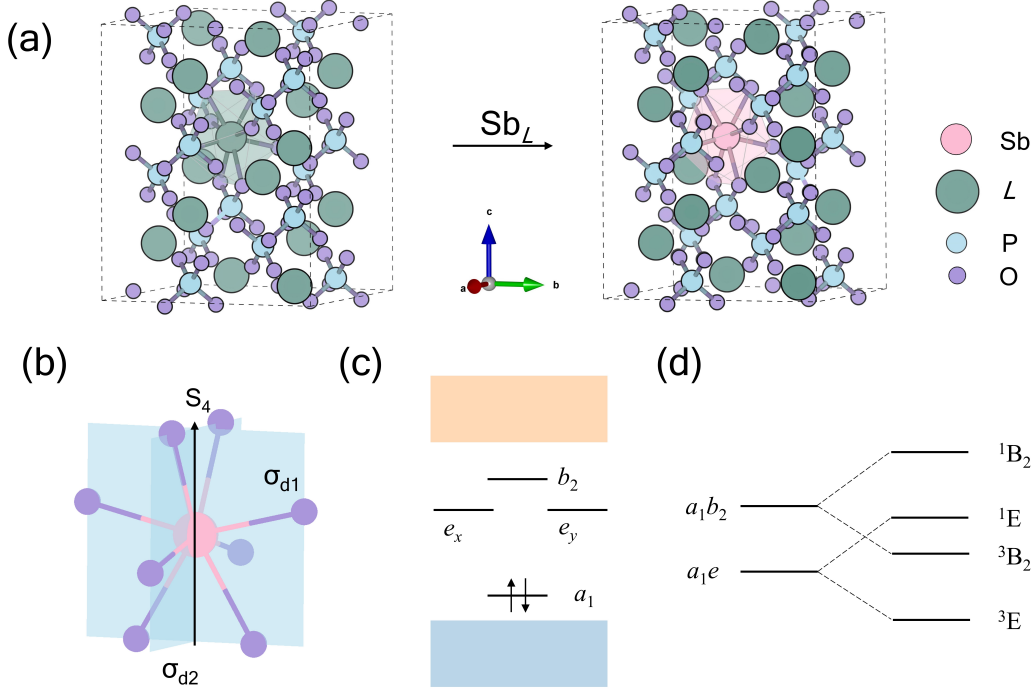


FIG. 1. (a) The left panel shows the crystal structure of LPO_4 ($L = Sc, Y, Lu$), and the right panel shows the structure of Sb^{3+} : LPO_4 . (b) The local structure of $[SbO_8]$, with $\sigma_{d1,2}$ representing two diagonal reflection planes. (c) A schematic illustration of the single-particle defect orbital levels within the band gap for the ground-state equilibrium structure, labeled according to the irreducible representations of the D_{2d} point group. (d) A schematic representation of the splitting of excited-state electron configurations a_1e and a_1b_2 into singlet and triplet states due to exchange interaction, without considering spin-orbit coupling.

the Brillouin zone of the supercells for calculations of hybrid functionals. The excited state equilibrium structures were optimized by PBEsol and PBE027 to compare the differences of these functionals. Calculations of dopant-related lowest excited states were performed by setting spin quantum numbers to a triplet state when spin-orbit coupling (SOC) was turned off, and by the constrained occupation method when SOC was included. To demonstrate that the effect of finite size can be ignored, we use Sb^{3+} -doped YPO_4 as an example and compare the results of supercells of two different sizes, as shown in Table S2 in the Supplemental Material [44].

To determine the energy barrier δ between the excited-state equilibrium structures, we utilized the climbing image nudged elastic band (CI-NEB) method [45, 46]. This method constructs the minimum energy path in atomic-configuration space by interpolating a series of interconnected images between the equilibrium structures.

D. Charge transition levels

The formation energy of a defect D in the charge state q is defined by [47]

$$E^f[D^q, E_F] = [E_{\text{tot}}[D^q] + E_{\text{corr}}] - E_{\text{tot}}[\text{bulk}] - \sum_i n_i \mu_i + qE_F, \quad (1)$$

where $E_{\text{tot}}[D^q]$ and $E_{\text{tot}}[\text{bulk}]$ are the calculated total energies of a supercell with or without defect D with charge q ; n_i represents the change in number of atom i due to defect D , which is added to ($n_i > 0$) or removed from ($n_i < 0$) the pristine supercell; μ_i is the chemical potential for atom i constrained by the coexistence of related substances, and E_F is the electron Fermi energy, which is determined by overall charge neutrality of all charged defects. The term E_{corr} is to correct the error in the supercell method under the periodic boundary condition in a practical DFT calculation. It usually includes two parts: the electrostatic image charge interaction and the potential alignment between the pristine supercells and the charged defect. The corrections that extend the scheme of Frysoldt, Neugebauer, and Van de Walle to an anisotropic medium (eFNV) are applied using the code developed by Kumagai [48–50].

The thermodynamic charge transition level (CTL) $\epsilon(q_1/q_2)$ is defined as the value of Fermi energy where the formation energies of charge states q_1 and q_2 are equal. From Eq. 1, we get

$$\epsilon(q_1/q_2) = \frac{E^f[D^{q_2}, 0] - E^f[D^{q_1}, 0]}{q_1 - q_2}. \quad (2)$$

In principle, the defect changes from the higher to the lower valences as the Fermi level increases across the

charge transition level. When $\epsilon(q_1/q_2)$ ($q_1 = q_2 + 1$) falls in the forbidden band, the gaps between $\epsilon(q_1/q_2)$ and band edges are the energies released when an electron and a hole are captured by D^{q_1} and D^{q_2} , respectively. To compare the positions of transition levels in different host materials, we selected the vacuum level as the potential energy zero point. The details of calculation of vacuum-referred binding energy (VRBE) are presented in the Supplemental Material [44].

E. Configuration coordinate diagrams

The interpolated structure \mathbf{R}_α between the initial equilibrium structure \mathbf{R}_α^i and the final equilibrium structure \mathbf{R}_α^f is obtained via linear interpolation. In the one-dimensional model adopted here, a signed generalized configuration coordinate Q is introduced for every interpolated structure, following Ref. [47, 51]:

$$Q^2 = \sum_{\alpha} m_{\alpha} (\mathbf{R}_{\alpha} - \mathbf{R}_{\alpha}^i)^2, \quad (3)$$

where m_{α} is the mass of atom α . Note that $Q = 0$ when \mathbf{R}_{α} corresponds to \mathbf{R}_{α}^i .

We employed the Δ SCF [52] method, which involves determining the excited-state equilibrium structure and computing the total energy of the (lowest) excited state relative to the ground state. Consequently, the configuration coordinate diagram was constructed and the energies of vertical transitions were obtained. We also examined the impact of spin-orbit coupling on excited-state dynamics, as antimony is a fourth period-post-transition metal. The energy and force tolerances were set to 10^{-5} eV and 0.01 eV/Å per atom, respectively.

III. RESULTS AND DISCUSSION

A. Hosts' geometric and electronic structures

LPO_4 ($L = \text{Sc, Y, Lu}$) belong to the tetragonal systems with $I4_1/\text{amd}$ space group (No. 141) [40], the crystal structure is shown as Figure 1(a). The metal ions L^{3+} are coordinated by eight oxygen atoms forming a dodecahedron with site symmetry D_{2d} . The $[LO_8]^{15-}$ polyhedra are connected by $[PO_4]^{3-}$ tetrahedra, and the $[LO_8]^{15-}$ polyhedra share edges with each other. Geometrically optimized lattice constants of LPO_4 with the PBEsol functional are in good agreement with the experimental values [40] and with previous calculated values for YPO_4 and $LuPO_4$ [39], as shown in Table I. The band gap of the hosts are calculated using PBEsol, PBE027, and GW_0 methods. The results reveal a significant underestimation of the band gap by PBEsol compared to experimental values and other computational approaches. In contrast, the band gap calculated using PBE027 is in

good agreement with both the GW_0 results and experimental measurements, thereby validating the appropriateness of our chosen α parameter. The band structure of LPO_4 obtained with GW_0 is shown in Figure S1 [44]. The electronic properties of the LPO_4 series are all similar. The valence bands are composed of O-p and the conduction bands are all composed of d orbitals for $ScPO_4$, YPO_4 , and $LuPO_4$. Further details of the results, along with the experimental values, are provided in Table S1 [44].

B. Group-theoretical analysis

In the ground state, the local environment of Sb^{3+} in LPO_4 exhibits D_{2d} symmetry. Upon excitation of Sb^{3+} , it rapidly undergoes non-radiative relaxation to approach the local equilibrium structures of the lowest electronic excited state (a_1e) 3E in Fig. 1(c,d). We consider the following two regimes of structure relaxations that lower the degeneracy and energy of 3E : (i) the Jahn-Teller effect, denoted as $E \otimes (b_1 + b_2)$, which reduces the symmetry to C_{2v} , and (ii) the pseudo Jahn-Teller effect [33], represented by $(B_2 + E) \otimes e$, which lowers the symmetry to C_2 . The capital letters represent the irreducible representations of electronic states, while lowercase letters denote the irreducible representations of vibrational modes.

It should be noted that the electron states couple to all vibrational modes at the same time. For simplicity and for a clearer picture, we have considered two independent cases governed by JT and pseudo-JT effects, where distortions are dominated by different vibration modes.

The dependence of the electron-nuclear interaction $V(r, Q)$ on Q can be expanded as [53],

$$\begin{aligned} W(r, Q) &= V(r, Q) - V(r, Q_0) \\ &= \sum_{\alpha} \frac{\partial V}{\partial Q_{\alpha}} Q_{\alpha} + \frac{1}{2} \sum_{\alpha\beta} \frac{\partial^2 V}{\partial Q_{\alpha} \partial Q_{\beta}} Q_{\alpha} Q_{\beta} + \dots \end{aligned} \quad (4)$$

The matrix elements of the expansion coefficients in Eq. (4) are called vibronic constants [53], which govern the changes in the electronic structure influenced by nuclear displacements or phonon modes.

For the $E \otimes (b_1 + b_2)$ regime, the linear electron-phonon coupling term combined with the parabolic vibrational potential determines the extrema points in the APES. Referring to Table V in Appendix A, the matrix representation of the linear term in Eq. (4) is:

$$W = \begin{bmatrix} F_2 Q_2 & F_1 Q_1 \\ F_1 Q_1 & -F_2 Q_2 \end{bmatrix}, \quad (5)$$

with

$$F_1 = \left\langle v \left| \left(\frac{\partial V}{\partial Q_{b_1}} \right) \right| u \right\rangle, \quad (6)$$

$$F_2 = \left\langle u \left| \left(\frac{\partial V}{\partial Q_{b_2}} \right) \right| u \right\rangle = - \left\langle v \left| \left(\frac{\partial V}{\partial Q_{b_2}} \right) \right| v \right\rangle. \quad (7)$$

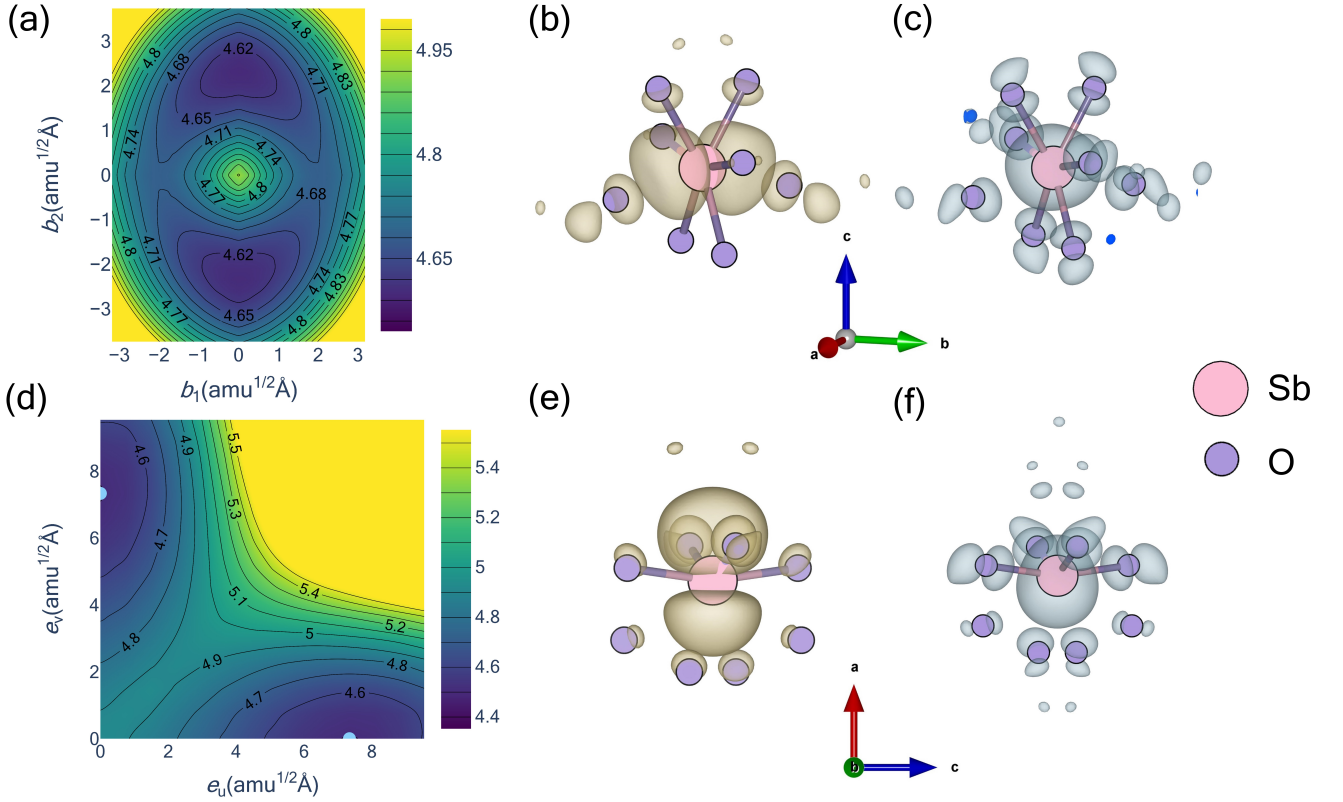


FIG. 2. (a), (d) The excited-state APES of Sb^{3+} in YPO_4 along the equivalent $b_{1,2}$ and $e_{u,v}$ modes, respectively, were obtained by the PBEsol functional. The calculations were performed by ΔSCF with setting spin quantum numbers without including SOC. The excited-state equilibrium structure was obtained by applying an initial distortion to the ground-state equilibrium structure, according to the vibrational modes described in the Appendix B. The squared orbital functions of the electron orbital (b), (e) and hole orbital (c), (f) were calculated at the equilibrium excited-state structures dominated by the distortion of the equivalent b_2 and e vibrational modes.

Here, $|u\rangle$ and $|v\rangle$ are the orbital wave functions of the two E states, which transform in the same way as the x and y components of a p orbital. The solution of the combination of Eq. (5) with the parabolic vibrational potential produces two pairs of equilibrium structures, one pair along the Q_{b_1} direction and the other along the Q_{b_2} direction.

For the regime $(^3\text{B}_2 + ^3\text{E}) \otimes e$, a Mexican hat-like potential energy surface is produced if only the linear vibronic constants are considered. By including the quadratic terms [53], the quantity defined by Eq. (4) can be written as the following matrix:

$$\begin{bmatrix} -\Delta + G_1(Q_u^2 - Q_v^2) & G_2Q_uQ_v & FQ_u \\ G_2Q_uQ_v & -\Delta - G_1(Q_u^2 - Q_v^2) & -FQ_v \\ FQ_u & -FQ_v & \Delta \end{bmatrix}, \quad (8)$$

where 2Δ denotes the energy gap between the $^3\text{B}_2$ (with the orbital wave function $|b_2\rangle$) and ^3E , F denotes the pseudo Jahn-Teller linear vibronic constant expressed as

$$F = \left\langle b_2 \left| \frac{\partial V}{\partial Q_u} \right| u \right\rangle = - \left\langle b_2 \left| \frac{\partial V}{\partial Q_v} \right| v \right\rangle, \quad (9)$$

and G_1 and G_2 are the pseudo Jahn-Teller quadratic vi-

bronic constants given as

$$2G_1 = \left\langle u \left| \frac{\partial^2 V}{\partial Q_u^2} \right| u \right\rangle = - \left\langle v \left| \frac{\partial^2 V}{\partial Q_v^2} \right| v \right\rangle, \quad (10)$$

$$2G_2 = \left\langle u \left| \frac{\partial^2 V}{\partial Q_u \partial Q_v} \right| v \right\rangle = \left\langle v \left| \frac{\partial^2 V}{\partial Q_u \partial Q_v} \right| u \right\rangle \quad (11)$$

In polar coordinates for the degenerate vibration modes, $Q_u = \rho \cos \phi$ and $Q_v = \rho \sin \phi$. The extrema points are at $\phi = n\pi/4$ ($n = 0, 1, 2, \dots, 7$). If $G_1 > G_2$, minima occur at $\phi = n\pi/4$ with even n , while odd n values form saddle points. Conversely, if $G_1 < G_2$, odd n values correspond to minima, while even n correspond to saddle points (see Chapter 4 of Ref [53]).

C. Verification via First-Principles Calculations

Using the model Hamiltonian for Jahn-Teller and pseudo Jahn-Teller effects, we have pinpointed the vibrational modes that significantly impact the potential energy surface. Interestingly, in the vibrational modes of the local structure $[\text{SbO}_8]$, the irreducible representations of the displacements of the central ion match those of

TABLE II. Excitation (exc.), emission (emi.), and their zero-phonon line (zpl) energies for Sb^{3+} in LPO_4 ($L = \text{Sc}, \text{Y}, \text{and Lu}$) calculated using PBEsol and PBE027 functions, together with experimental results (in units of eV). Here, JT and pJT denote the equilibrium structures of the excited states associated with the Jahn-Teller and pseudo Jahn-Teller effects, respectively, while the JT* here represents the equilibrium structure obtained by applying a small distortion to the JT equilibrium structure towards the pJT equilibrium structure.

LPO_4		PBEsol							PBE027							Exp. [30, 31]	
		JT			JT*		pJT		JT			JT*		pJT			
		exc.	zpl	emi.	zpl	emi.	zpl	emi.	exc.	zpl	emi.	zpl	emi.	zpl	emi.		
with SOC	Sc	/							5.02 ^a	4.79	4.42	/		4.63	2.91	5.17	4.13, 3.40
	Y	4.63	4.51	4.21	4.47	3.98	4.45	3.15	4.94	4.67	4.20	4.59	3.89	4.44	2.43	5.06	4.28, 2.99
	Lu	4.72	4.63	4.39	4.58	4.08	4.55	3.40	5.02	4.80	4.37	4.71	4.03	4.61	2.72	5.06	4.28, 3.10
without SOC	Sc	/							5.32 ^a	/				4.66	2.89	5.17	4.13, 3.40
	Y	4.91	4.60	4.23	4.55	3.96	4.50	3.10	5.25	4.74	4.26	4.65	3.90	4.48	2.44	5.06	4.28, 2.99
	Lu	5.02	4.74	4.42	4.66	4.07	4.61	3.33	5.33	4.88	4.42	4.77	4.04	4.64	2.74	5.06	4.28, 3.10

^a Estimated by the energy difference of $ns \rightarrow np$ single-electron excitation calculated at the equilibrium structure of the ground state.

the vibration modes involved in the Jahn-Teller (b_2) and pseudo Jahn-Teller effects (e), as shown in Appendix B. Consequently, by starting from geometric structures with different initial displacements of the central ion over the equilibrium geometric structure of the ground state, we obtained different (constrained) excited-state equilibrium geometric structures, i.e., minima on the APES, dominated by displacements of different equivalent modes. It is important to note, however, that in real systems, there may be multiple vibrational modes that correspond to the same irreducible representation, as shown in Appendix B. Therefore, the aforementioned analysis of vibration modes can be understood as being based on effective vibration modes composed of many modes of the irreducible representation of the point group.

The LPO_4 series are isostructure and contain only one site for L . Hence, we take Sb^{3+} in YPO_4 as an example to demonstrate how the two excited-state local minima dominated by the Jahn-Teller and the pseudo Jahn-Teller effects individually affect the potential energy surface.

Consistent with the analysis of the regime involving the Jahn-Teller effect, as illustrated in Figure 2 (a), the results of first-principles calculations reveal the presence of extrema on the APES along the equivalent b_1 and b_2 modes. Specifically, there is a pair of equivalent minima along the b_2 mode, where the symmetry of the system decreases from D_{2d} to C_{2v} , while a pair of equivalent saddle points appears along the b_1 axis. The squared orbital functions of the electron (with component Sb-5p) and hole (with component Sb-5s) at the equilibrium excited-state structure dominated by the equivalent b_2 mode are shown in Figure 2 (b, c). In Figure 2 (d), we present the APES resulting from the pseudo Jahn-Teller effect, and the squared orbital functions of the electron (Sb-5p) and hole (Sb-5s) at the equilibrium excited-state structure dominated by the equivalent e mode are shown in

Figure 2 (e, f). Following the analysis of the regime involving the pseudo Jahn-Teller effect, we obtained four equivalent excited-state structures with the same minimal energy, which correspond to slight structural distortions of the central ion along the $(+x, +y)$, $(+x, -y)$, $(-x, +y)$, and $(-x, -y)$ directions, where the symmetry decreases from D_{2d} to C_2 . To simplify the computation, we selected two of these structures to construct the APES. The calculation results are in agreement with our expectations. In general, the APES dominated by the Jahn-Teller effect and the pseudo Jahn-Teller effect exhibit significant differences. According to the characteristics of the excited-state structures dominated by the two different modes, we term the excited-state configuration dominated by the b_2 mode as the “high-symmetry configuration”, labeled as JT, and the one dominated by the e mode as the “off-center configuration”, labeled as pJT. The vertical transition energies between JT and pJT, as well as the zero-phonon line energies, are summarized in Table II.

Although these results align well with the group-theoretical analysis presented in the previous section, it is important to note that couplings to different vibration modes coexist. Therefore, the stability of the obtained structures must be verified against small symmetry-breaking distortions. When ionic relaxation was initiated with these distortions applied to the Jahn-Teller (JT) structure, a new excited-state equilibrium structure with C_1 symmetry, referred to as JT*, was achieved. As indicated in Table III, the JT* structure exhibits an average Sb-O bond length that closely resembles that of the JT structure. Furthermore, the root-mean-square deviation of the Sb-O bond lengths in the JT* structure, relative to the ground-state equilibrium structure, is also very close to that of the JT structure. This indicates that the JT* excited-state equilibrium structure remains predom-

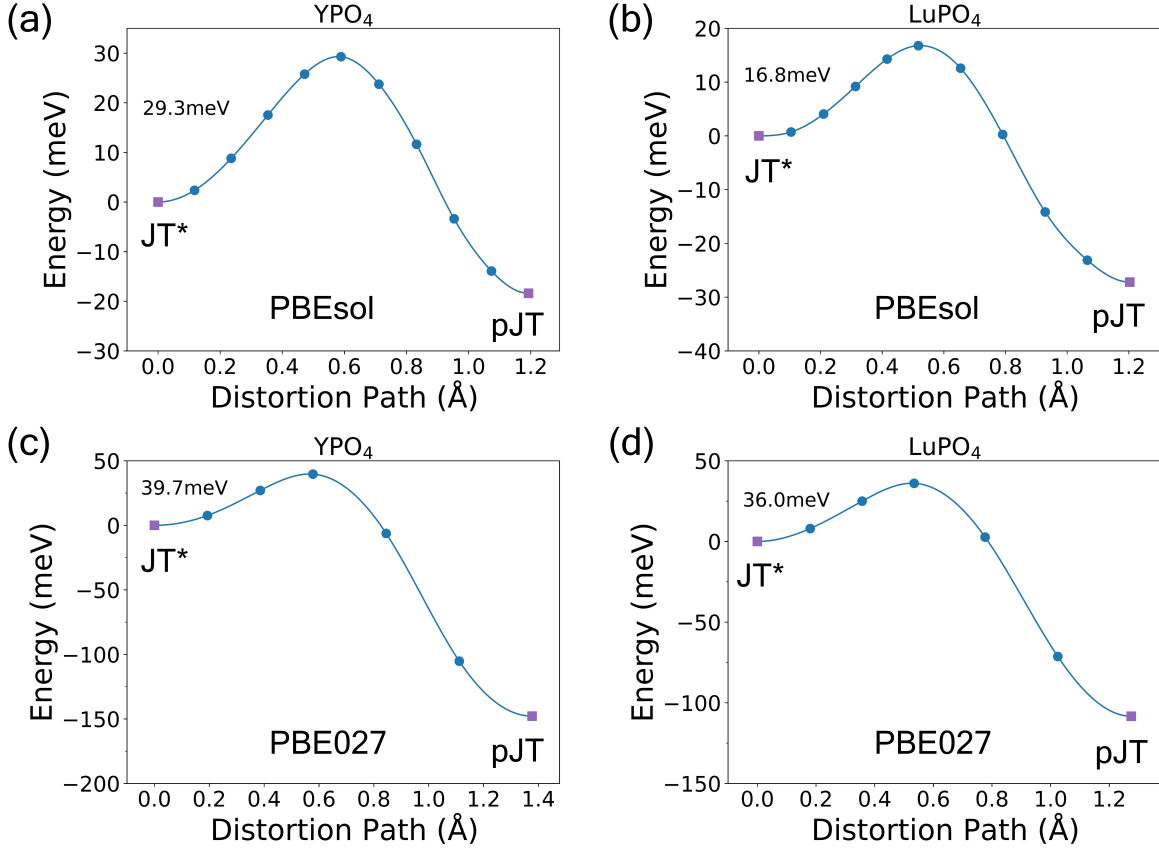


FIG. 3. Energy barriers between JT* and the pJT of YPO₄ (a,c) and LuPO₄ (b,d) calculated using the climbing image nudged elastic band (CI-NEB) method [45, 46], including SOC. For the PBEsol functional, 9 images were inserted between the two equilibrium structures, while for the PBE027 hybrid functional, 5 images were used.

inantly governed by the Jahn-Teller effect. Moreover, the pJT structure is stable as it is essentially recovered after ionic relaxation from configurations with small introduced distortions.

To further verify that the JT* structure is not a saddle point and to quantitatively determine the energy barrier between JT* and pJT, we employed the CI-NEB method [45, 46]. For the PBEsol calculations, we inserted 9 images, whereas for the computational more intensive PBE027 calculations, we used 5 images, as shown in Figure 3. We find that the energy barrier δ and zero-phonon line energy difference ΔE_{zpl} are functional-dependent. Detailed information on the energy barrier δ and the zero-phonon line energy difference ΔE_{zpl} between JT* and pJT is provided in Table IV. In the YPO₄ system, the barrier calculated using PBEsol is 29.3 meV, while that obtained with PBE027 is 39.7 meV. Both results are in satisfactory agreement with the experimental results [30, 31]. However, the magnitude of ΔE_{zpl} differs significantly between the two functionals: PBEsol gives 18 meV, whereas PBE027 gives 148 meV. The PBEsol value deviates substantially from the experimental data, while the PBE027 result shows closer agreement. Moreover, the energy barrier between JT* and pJT obtained

without considering SOC is found to be similar to that calculated with SOC included, as shown in Figure S4 [44] and Figure 3. This indicates that the inclusion of spin-orbit coupling has a relatively minor effect on the energy barrier between these two configurations.

Despite the fact that the PBEsol underestimates the bandgap of YPO₄, the calculated vertical transition energies of Sb³⁺ in YPO₄ align well with the experimental results [30, 31], as shown in Table II. The PBE027 hybrid functional also gives reasonable results, but the calculated emission energies of the pJT are underestimated compared to the experimental values, similar to the case with halide systems [27–29]. This suggests that the vertical transition energies calculated at the excited-state equilibrium structures dominated by the *e* mode distortion are more sensitive to the choice of the fraction of exact exchange in the hybrid functional, α , than those calculated at those equilibrium structures dominated by the *b*₂ mode distortion. In the case of polarons, Sio et al. indicated that the formation energy of polaron increases with α (see Supplemental Note 1 in [54]). However, for excitons or excitonic polarons [55, 56], crystal structure distortions due to electron-hole interactions may not uniformly impact the excited- and ground-state structures.

TABLE III. Average bond length \bar{l} (Å) of Sb-O bonds in the $[\text{SbO}_8]$ local structure for different equilibrium configurations, along with the root-mean-square deviation Δl (Å) of bond lengths between excited-state and ground-state configurations ($\Delta l = \sqrt{\frac{1}{8} \sum_i (l_i^{\text{ES}} - l_i^{\text{GS}})^2}$), including SOC.

	$L\text{PO}_4$	GS	JT		JT*		pJT	
		\bar{l}	\bar{l}	Δl	\bar{l}	Δl	\bar{l}	Δl
PBEsol	Y	2.360	2.368	0.08	2.379	0.13	2.440	0.27
	Lu	2.332	2.334	0.07	2.348	0.12	2.385	0.22
PBE027	Sc	2.302	2.283	0.08	/		2.369	0.28
	Y	2.362	2.362	0.10	2.375	0.16	2.491	0.41
	Lu	2.332	2.331	0.09	2.346	0.14	2.427	0.33

A detailed examination of this scenario extends beyond the focus of this paper and will not be further elaborated upon here.

D. Impact of spin-orbit coupling

SOC has a profound influence on the energy level structure of a free Sb^{3+} ion [21]. However, within a crystal lattice, the interplay between SOC and the structural distortions induced by the Jahn-Teller effect tends to suppress the effect of SOC [57, 58]. Consequently, the calculated emission energies of Sb^{3+} in $L\text{PO}_4$ are not significantly affected by inclusion of SOC, as shown in Table II.

Although Bi^{3+} shares a similar electronic configuration with Sb^{3+} , the optical properties of Bi: YPO_4 and LuPO_4 [39, 59–61] and their variation with temperature exhibit distinct characteristics compared to those of Sb: YPO_4 and LuPO_4 . This variation arises from the substantial difference in the strength of SOC, ξ . By utilizing virtual Kohn-Sham orbitals, we can estimate the SOC strength [39]. For instance, the SOC parameter, ξ , is calculated to be 0.47 eV for Sb: YPO_4 , but a much larger value of 1.27 eV is obtained for Bi: YPO_4 . The striking difference in SOC parameters leads to significant alterations in the potential energy surfaces [58], which in turn influence the optical properties.

E. Differences among the $L\text{PO}_4$ series

To clarify the differences among the three systems, we computed the thermodynamic charge transition levels, as depicted in Figure 4. Figure 4 demonstrates that the thermodynamic charge transition level of (0/1-) in the ScPO_4 system is notably closer to the conduction band minimum (CBM) than in the other two systems, indicating a higher probability of Sb^{3+} ionization in ScPO_4 . Ad-

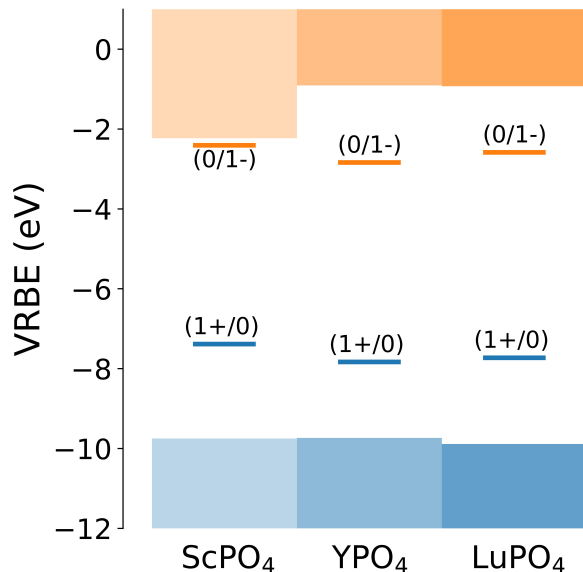


FIG. 4. Vacuum referred binding energy of thermodynamic charge transition levels of Sb^{3+} in $L\text{PO}_4$ ($L = \text{Sc}, \text{Y}, \text{Lu}$) calculated by PBE027.

ditionally, we attempted to introduce a small distortion to the JT structure of Sb^{3+} : ScPO_4 along the direction of the pJT structure. However, during structural optimization, the electron tended to relax into the conduction band, preventing the attainment of a JT* structure analogous to those observed in the YPO_4 and LuPO_4 systems. This behavior is attributed to the fact that the transition level of Sb^{3+} (0/1-) lies very close to the conduction band. In contrast, for the Y/Lu PO_4 systems, the thermodynamic charge transition levels of Sb^{3+} are farther from the band edges, resulting in superior luminescent properties compared to ScPO_4 [30, 31].

Furthermore, we examined the variations in the average bond length \bar{l} of Sb-O bonds within the $[\text{SbO}_8]$ local structure for different equilibrium configurations, as well as the root-mean-square deviation Δl of bond lengths between excited-state and ground-state configurations, as shown in Table III. For the JT and JT* structures, the Δl values across the three systems $L\text{PO}_4$ are found to be relatively similar and show little correlation with the host L^{3+} cation. In contrast, for the pJT structure, YPO_4 displays the largest deviation from the ground-state equilibrium configuration, regardless of whether calculated using PBEsol or PBE027.

In the LuPO_4 system, the energy barrier between JT* and pJT calculated using the CI-NEB method is smaller than that in the YPO_4 system, as shown in Table IV and Figure 3. Notably, the barrier obtained with PBEsol in the LuPO_4 system is only about half of that in the YPO_4 system. This suggests that at low temperatures, the LuPO_4 system is more likely to relax from the JT* structure to the pJT structure. This finding is consistent with experimental observations, where both the “UV

TABLE IV. The calculated and experimental values of the energy barrier δ between JT* and pJT, as well as the zero-phonon line energy difference ΔE_{zpl} (in units of meV). For the ScPO_4 , the ΔE_{zpl} between JT and pJT is used as an estimate.

$L\text{PO}_4$	δ			ΔE_{zpl}		
	PBEsol	PBE027	Exp.	PBEsol	PBE027	Exp.
Sc	/	/	/	/	166	74 [30], 72 [31]
Y	29.3	39.7	10.0 [30], 40.9 [31]	18	148	129 [30], 107 [31]
Lu	16.8	36.0	5.0 [30]	27	108	99 [30], 102 [31]

band” and “visible band” are simultaneously detected at low temperatures [30, 31].

IV. CONCLUSIONS

Our calculations reveal that the dual-band emissions of Sb^{3+} in the $L\text{PO}_4$ series are primarily governed by two sets of distinct excited-state local minima. These arise from distortions primarily governed by two different set of effective vibration modes via the Jahn-Teller effect and the pseudo Jahn-Teller effect. The two distinct sets of equilibrium structures for excited states give rise to the experimentally observed “UV band” (JT) and the “visible band” (pJT). The relative position of the charge transition levels to the host bands significantly impacts the optical properties of the dopant ions. In particular, the differences in the host cations can influence the energy barriers between different excited-state equilibrium structures, thereby affecting the relative intensities of the “UV band” and the “visible band” at low temperatures. In contrast to $6s^2$ dopant, such as Bi^{3+} , the influence of SOC on the potential energy surface of the $5s^2$ dopant, Sb^{3+} , remains largely suppressed by the Jahn-Teller effect. This means that SOC is not significant in determining the adiabatic potential energy surface of Sb^{3+} , although it is deemed important in lifting the spin-forbiddness in optical transitions. This study demonstrates that the interplay of ligand fields, vibration modes, and spin-orbit interactions may lead to rich phenomena in excited state dynamics.

ACKNOWLEDGMENTS

This work was supported by the National Natural Science Foundation of China (Grants No. 12474242 and No. 62375255), the Innovation Program for Quantum Science and Technology (Grant No. 2021ZD0302200), and University Science Research Project of Anhui Province

(Grant No. KJ2020A0820). The numerical calculations were partially performed on the supercomputing system at the Supercomputing Center of the University of Science and Technology of China.

Appendix A: Clebsch-Gordan Coefficients

TABLE V. Clebsch-Gordan coefficients of $E \otimes E$ in D_{2d} point group

$E \otimes E$		A_1	A_2	B_1	B_2
γ_1	γ_2				
u	u	$\frac{1}{\sqrt{2}}$	0	0	$\frac{1}{\sqrt{2}}$
	v	0	$\frac{1}{\sqrt{2}}$	$\frac{1}{\sqrt{2}}$	0
v	u	0	$-\frac{1}{\sqrt{2}}$	$\frac{1}{\sqrt{2}}$	0
	v	$\frac{1}{\sqrt{2}}$	0	0	$-\frac{1}{\sqrt{2}}$

TABLE VI. Clebsch-Gordan coefficients of $B_1 \otimes E$ in D_{2d} point group

$B_1 \otimes E$		E	
γ_1	γ_2	u	v
b_1	u	0	1
	v	1	0

TABLE VII. Clebsch-Gordan coefficients of $B_2 \otimes E$ in D_{2d} point group

$B_2 \otimes E$		E	
γ_1	γ_2	u	v
b_2	u	1	0
	v	0	-1

Appendix B: Vibrational Modes

In this section, we list the vibrational modes of $[\text{SbO}_8]$ in Sb: $L\text{PO}_4$. The local structure of $[\text{SbO}_8]$ is shown as in Fig. 5

$$\text{Sb:} \begin{cases} B_2 : z_0 \\ E : \begin{cases} x_0 \\ y_0 \end{cases} \end{cases}$$

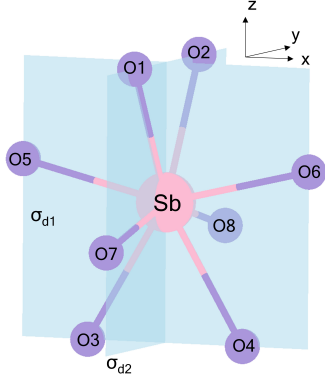


FIG. 5. The SbO_8 local structure in Sb: LPO_4 and $\sigma_{d1,2}$ represent two diagonal reflection planes of the point group D_{2d} . For convenience, we establish a new coordinate system so that x -axis and y -axis are normal to the reflection planes σ_{d2} and σ_{d1} , respectively.

$$E : \left\{ \begin{array}{l} E_1 \left\{ \begin{array}{l} -O_{1z} + O_{2z} \\ O_{3z} - O_{4z} \end{array} \right. \\ E_2 \left\{ \begin{array}{l} O_{5z} - O_{6z} \\ -O_{7z} + O_{8z} \end{array} \right. \\ E_3 \left\{ \begin{array}{l} O_{1x} + O_{2x} - O_{3x} - O_{4x} \\ -O_{1y} - O_{2y} + O_{3y} + O_{4y} \end{array} \right. \\ E_4 \left\{ \begin{array}{l} O_{5x} + O_{6x} - O_{7x} - O_{8x} \\ -O_{5y} - O_{6y} + O_{7y} + O_{8y} \end{array} \right. \\ E_5 \left\{ \begin{array}{l} O_{1x} + O_{2x} + O_{3x} + O_{4x} \\ O_{1y} + O_{2y} + O_{3y} + O_{4y} \end{array} \right. \\ E_6 \left\{ \begin{array}{l} O_{5x} + O_{6x} + O_{7x} + O_{8x} \\ O_{5y} + O_{6y} + O_{7y} + O_{8y} \end{array} \right. \end{array} \right.$$

$$A_1 : \left\{ \begin{array}{l} O_{1z} + O_{2z} - O_{3z} - O_{4z} \\ O_{5z} + O_{6z} - O_{7z} - O_{8z} \\ O_{1y} - O_{2y} + O_{3x} - O_{4x} \\ O_{5x} - O_{6x} + O_{7y} - O_{8y} \end{array} \right.$$

$$A_2 : \left\{ \begin{array}{l} -O_{1x} + O_{2x} + O_{3y} - O_{4y} \\ O_{5y} - O_{6y} - O_{7x} + O_{8x} \end{array} \right.$$

$$B_1 : \left\{ \begin{array}{l} O_{1x} - O_{2x} + O_{3y} - O_{4y} \\ O_{5y} - O_{6y} + O_{7x} - O_{8x} \end{array} \right.$$

$$B_2 : \left\{ \begin{array}{l} O_{1z} + O_{2z} + O_{3z} + O_{4z} \\ O_{5z} + O_{6z} + O_{7z} + O_{8z} \\ -O_{1y} + O_{2y} + O_{3x} - O_{4x} \\ O_{5x} - O_{6x} - O_{7y} + O_{8y} \end{array} \right.$$

- [1] J. Li, H. Liang, C. Xiao, X. Jia, R. Guo, J. Chen, X. Guo, R. Luo, X. Wang, M. Li, M. Rossier, A. Hauser, F. Linardi, E. Alvianto, S. Liu, J. Feng, and Y. Hou, Enhancing the Efficiency and Longevity of Inverted Perovskite Solar Cells with Antimony-Doped Tin Oxides, *Nature Energy* **9**, 308 (2023).
- [2] T. Wang, H.-L. Loi, Q. Cao, Z. Feng, Guitao and Guan, Q. Wei, C. Chen, M. Li, Y. Zhu, C.-S. Lee, and F. Yan, Counter-Doping Effect by Trivalent Cations in Tin-Based Perovskite Solar Cells, *Advanced Materials*, 2402947 (2024).
- [3] B. Zhang, Y. Ru, J. Zhou, J. Jia, H. Song, Z. Liu, L. Zhang, X. Liu, G.-M. Zhong, X. Yong, I. R. Panneerselvam, L. Manna, and S. Lu, A Robust Anti-Thermal-Quenching Phosphor Based on Zero-Dimensional Metal Halide $\text{Rb}_3\text{InCl}_6\text{:xSb}^{3+}$, *Journal of the American Chemical Society* **146**, 7658 (2024).
- [4] R. Zeng, L. Zhang, Y. Xue, B. Ke, Z. Zhao, D. Huang, Q. Wei, W. Zhou, and B. Zou, Highly Efficient Blue Emission from Self-Trapped Excitons in Stable Sb^{3+} -Doped $\text{Cs}_2\text{NaInCl}_6$ Double Perovskites, *The Journal of Physical Chemistry Letters* **11**, 2053 (2020).
- [5] Z. Li, Y. Li, P. Liang, T. Zhou, L. Wang, and R.-J. Xie, Dual-Band Luminescent Lead-Free Antimony Chloride Halides with Near-Unity Photoluminescence Quantum Efficiency, *Chemistry of Materials* **31**, 9363 (2019).
- [6] Y. Jing, Y. Liu, X. Jiang, M. S. Molokeev, Z. Lin, and Z. Xia, Sb^{3+} Dopant and Halogen Substitution Triggered Highly Efficient and Tunable Emission in Lead-Free Metal Halide Single Crystals, *Chemistry of Materials* **32**, 5327 (2020).
- [7] B. Su, S. Geng, Z. Xiao, and Z. Xia, Highly Distorted Antimony(III) Chloride $[\text{Sb}_2\text{Cl}_8]^{2-}$ Dimers for Near-Infrared Luminescence up to 1070nm, *Angewandte Chemie International Edition* **61**, e202208881 (2022).
- [8] B. Su, M. Li, E. Song, and Z. Xia, Sb^{3+} -Doping in Cesium Zinc Halides Single Crystals Enabling High-Efficiency Near-Infrared Emission, *Advanced Functional Materials* **31**, 2105316 (2021).
- [9] J.-C. Jin, Y. Peng, Y. Xu, K. Han, A.-R. Zhang, X.-B. Yang, and Z. Xia, Bright Green Emission from Self-Trapped Excitons Triggered by Sb^{3+} Doping in Rb_4CdCl_6 , *Chemistry of Materials* **34**, 5717 (2022).
- [10] A. Wolfert and G. Blasse, Luminescence of Bi^{3+} -Doped Crystals of $\text{Cs}_2\text{NaYBr}_6$ and $\text{Cs}_2\text{NaLaCl}_6$, *Journal of Solid State Chemistry* **59**, 133 (1985).
- [11] J. D. Majher, M. B. Gray, T. Liu, N. P. Holzapfel, and P. M. Woodward, Rb_3InCl_6 : A Monoclinic Double Perovskite Derivative with Bright Sb^{3+} -Activated Photoluminescence, *Inorganic Chemistry* **59**, 14478 (2020).
- [12] A. Nocolak, V. Morad, K. M. McCall, S. Yakunin, Y. Shynkarenko, M. Wörle, and M. V. Kovalenko, Bright Blue and Green Luminescence of Sb(III) in Double Perovskite $\text{Cs}_2\text{MInCl}_6$ ($\text{M} = \text{Na}, \text{K}$) Matrices, *Chemistry of Materials* **32**, 5118 (2020).
- [13] F. Locardi, M. Samoli, A. Martinelli, O. Erdem, D. V. Magalhaes, S. Bals, and Z. Hens, Cyan Emission in Two-Dimensional Colloidal $\text{Cs}_2\text{CdCl}_4\text{:Sb}^{3+}$ Ruddlesden-Popper Phase Nanoplatelets, *ACS Nano* **15**, 17729 (2021).
- [14] E. W. J. L. Oomen, W. M. A. Smit, and G. Blasse, On the Luminescence of Sb^{3+} in $\text{Cs}_2\text{NaMCl}_6$ (with $\text{M} = \text{Sc}, \text{Y}, \text{La}$): A Model System for the Study of Trivalent s^2 Ions, *Journal of Physics C: Solid State Physics* **19**, 3263 (1986).
- [15] Y. Jing, Y. Liu, J. Zhao, and Z. Xia, Sb^{3+} Doping-Induced Triplet Self-Trapped Excitons Emission in Lead-Free Cs_2SnCl_6 Nanocrystals, *The Journal of Physical Chemistry Letters* **10**, 7439 (2019).
- [16] B. Chen, Y. Guo, Y. Wang, Z. Liu, Q. Wei, S. Wang, A. L. Rogach, G. Xing, P. Shi, and F. Wang, Multi-excitonic Emission in Zero-Dimensional $\text{Cs}_2\text{ZrCl}_6\text{:Sb}^{3+}$ Perovskite Crystals, *Journal of the American Chemical Society* **143**, 17599 (2021).
- [17] R. Liu, W. Zhang, G. Li, and W. Liu, Excitation Wavelength Tunable White Light Emission in Vacancy-Ordered Double Perovskite, *Chemical Communications* **57**, 10943 (2021).
- [18] X. Meng, Q. Wei, W. Lin, T. Huang, S. Ge, Z. Yu, and B. Zou, Efficient Yellow Self-Trapped Exciton Emission in Sb^{3+} -Doped RbCdCl_3 Metal Halides, *Inorganic Chemistry* **61**, 7143 (2022).
- [19] S. Ge, H. Peng, Q. Wei, X. Shen, W. Huang, W. Liang, J. Zhao, and B. Zou, Realizing Color-Tunable and Time-Dependent Ultralong Afterglow Emission in Antimony-Doped CsCdCl_3 Metal Halide for Advanced Anti-Counterfeiting and Information Encryption, *Advanced Optical Materials* **11**, 2300323 (2023).
- [20] J. Zhou, C. Shi, X. Li, Z. Sun, Y. Ji, J. Deng, and B. Wang, A Heterovalent Doping Strategy Induced Efficient Cyan Emission in Sb^{3+} -Doped CsCdCl_3 Perovskite Microcrystal for Solid State Lighting, *Ceramics International* **48**, 28327 (2022).
- [21] Y. Jing, Y. Liu, M. Li, and Z. Xia, Photoluminescence of Singlet/Triplet Self-Trapped Excitons in Sb^{3+} -Based Metal Halides, *Advanced Optical Materials* **9**, 2002213 (2021).
- [22] H. Arfin and A. Nag, Origin of Luminescence in Sb^{3+} - and Bi^{3+} -Doped Cs_2SnCl_6 Perovskites: Excited State Relaxation and Spin-Orbit Coupling, *The Journal of Physical Chemistry Letters* **12**, 10002 (2021).
- [23] Z. Gong, W. Zheng, P. Huang, X. Cheng, W. Zhang, M. Zhang, S. Han, and X. Chen, Highly Efficient Sb^{3+} Emitters in 0D Cesium Indium Chloride Nanocrystals with Switchable Photoluminescence Through Water-Triggered Structural Transformation, *Nano Today* **44**, 101460 (2022).
- [24] D. Zhao, Y. Liu, Y. Han, X. Chen, M. Jia, J. Zhang, L. Lian, D. Wu, X. Li, and Z. Shi, Tunable White Light Emission in Antimony Doped Vacancy-Ordered Double Perovskite Cs_2ZrCl_6 nanocrystals, *Journal of Luminescence* **270**, 120548 (2024).
- [25] A. Fukuda, Jahn-Teller Effect on the Structure of the Emission Produced by Excitation in the A Band of KI: Tl -Type Phosphors. Two Kinds of Minima on the $\Gamma_4^- (^3T_{1u})$ Adiabatic Potential-Energy Surface, *Physical Review B* **1**, 4161 (1970).
- [26] M. Liu, C.-K. Duan, P. A. Tanner, C.-G. Ma, and M. Yin, Rationalizing the Photoluminescence of Bi^{3+} and Sb^{3+} in Double Perovskite Halide Crystals, *The Journal of Physical Chemistry C* **125**, 26670 (2021).
- [27] M. Liu, C.-K. Duan, P. A. Tanner, C.-G. Ma, X. Wei, and M. Yin, Understanding Photoluminescence of Cs_2ZrCl_6

- Doped with Post-Transition-metal Ions Using First-Principles Calculations, *Phys. Rev. B* **105**, 195137 (2022).
- [28] R. Hao and C.-K. Duan, Unraveling the Photoluminescent Properties of Sb-Doped Cd-Based Inorganic Halides: A First-Principles Study, *Inorganic Chemistry* **63**, 3152 (2024).
- [29] R. Hao, M. Liu, M. Yin, and C.-K. Duan, Luminescence Mechanism of ns^2 Ions in $\text{Cs}_2(\text{Sn}/\text{Hf})\text{Cl}_6$ Revealed by First-Principles Calculations, *Journal of Physical Chemistry C* **127**, 3742 (2023).
- [30] E. Oomen, W. Smit, and G. Blasse, Jahn-Teller Effect in the Sb^{3+} Emission in Zircon-Structured Phosphates, *Chemical Physics Letters* **112**, 547 (1984).
- [31] E. W. J. L. Oomen, W. M. A. Smit, and G. Blasse, Jahn-Teller Effect in the Emission and Excitation Spectra of the Sb^{3+} Ion in LPO_4 ($\text{L}=\text{Sc}, \text{Lu}, \text{Y}$), *Phys. Rev. B* **37**, 18 (1988).
- [32] I. B. Bersuker, Pseudo-Jahn-Teller Effect-A Two-State Paradigm in Formation, Deformation, and Transformation of Molecular Systems and Solids, *Chemical Reviews* **113**, 1351 (2013).
- [33] I. B. Bersuker, Jahn-Teller and Pseudo-Jahn-Teller Effects: From Particular Features to General Tools in Exploring Molecular and Solid State Properties, *Chemical Reviews* **121**, 1463 (2021).
- [34] P. E. Blöchl, Projector Augmented-Wave Method, *Physical Review B* **50**, 17953 (1994).
- [35] G. Kresse and J. Hafner, *Ab initio* Molecular Dynamics for Open-Shell Transition Metals, *Physical Review B* **48**, 13115 (1993).
- [36] G. Kresse and J. Hafner, *Ab initio* Molecular-Dynamics Simulation of the Liquid-Metal-Amorphous-Semiconductor Transition in Germanium, *Physical Review B* **49**, 14251 (1994).
- [37] J. P. Perdew, A. Ruzsinszky, G. I. Csonka, O. A. Vydrov, G. E. Scuseria, L. A. Constantin, X. Zhou, and K. Burke, Restoring the Density-Gradient Expansion for Exchange in Solids and Surfaces, *Phys. Rev. Lett.* **100**, 136406 (2008).
- [38] V. Wang, N. Xu, J.-C. Liu, G. Tang, and W.-T. Geng, Vaspkit: A user-friendly interface facilitating high-throughput computing and analysis using vasp code, *Computer Physics Communications* **267**, 108033 (2021).
- [39] Z. Feng, B. Lou, M. Yin, Y.-y. Yeung, H.-T. Sun, and C.-K. Duan, First-Principles Study of Bi^{3+} -Related Luminescence and Electron and Hole Traps in $(\text{Y}/\text{Lu}/\text{La})\text{PO}_4$, *Inorganic Chemistry* **60**, 4434 (2021).
- [40] W. Milligan, D. Mullica, G. Beall, and L. Boatner, Structural Investigations of YPO_4 , ScPO_4 , and LuPO_4 , *Inorganica Chimica Acta* **60**, 39 (1982).
- [41] Y. Hinuma, G. Pizzi, Y. Kumagai, F. Oba, and I. Tanaka, Band structure diagram paths based on crystallography, *Computational Materials Science* **128**, 140 (2017).
- [42] L. Hedin, New Method for Calculating the One-Particle Green's Function with Application to the Electron-Gas Problem, *Phys. Rev.* **139**, A796 (1965).
- [43] M. S. Hybertsen and S. G. Louie, Electron Correlation in Semiconductors and Insulators: Band Gaps and Quasiparticle Energies, *Phys. Rev. B* **34**, 5390 (1986).
- [44] See Supplemental Material at [URL will be inserted by publisher] for detailed information on GW_0 band structures, demonstration of the absence of finite-size effects, VRBE, bond length of $[\text{SbO}_8]$ and barriers without including SOC, which contains Refs. 26, 30, 31, 43, 62–64.
- [45] G. Henkelman, B. P. Uberuaga, and H. Jónsson, A Climbing Image Nudged Elastic Band Method for Finding Saddle Points and Minimum Energy Paths, *The Journal of Chemical Physics* **113**, 9901–9904 (2000).
- [46] G. Henkelman and H. Jónsson, Improved Tangent Estimate in the Nudged Elastic Band Method for Finding Minimum Energy Paths and Saddle Points, *The Journal of Chemical Physics* **113**, 9978 (2000).
- [47] C. Freysoldt, B. Grabowski, T. Hickel, J. Neugebauer, G. Kresse, A. Janotti, and C. G. Van de Walle, First-Principles Calculations for Point Defects in Solids, *Reviews of Modern Physics* **86**, 253 (2014).
- [48] C. Freysoldt, J. Neugebauer, and C. G. Van de Walle, Fully *Ab Initio* Finite-Size Corrections for Charged-Defect Supercell Calculations, *Phys. Rev. Lett.* **102**, 016402 (2009).
- [49] Y. Kumagai and F. Oba, Electrostatics-Based Finite-Size Corrections for First-Principles Point Defect Calculations, *Phys. Rev. B* **89**, 195205 (2014).
- [50] Y. Kumagai, N. Tsunoda, A. Takahashi, and F. Oba, Insights into Oxygen Vacancies from High-Throughput First-Principles Calculations, *Physical Review Materials* **5**, 123803 (2021).
- [51] A. Alkauskas, Q. Yan, and C. G. Van de Walle, First-Principles Theory of Nonradiative Carrier Capture via Multiphonon Emission, *Phys. Rev. B* **90**, 075202 (2014).
- [52] R. O. Jones and O. Gunnarsson, The Density Functional Formalism, Its Applications and Prospects, *Rev. Mod. Phys.* **61**, 689 (1989).
- [53] I. B. Bersuker, *The Jahn-Teller Effect* (Cambridge University Press, Cambridge, 2006).
- [54] W. H. Sio and F. Giustino, Polarons in Two-Dimensional Atomic Crystals, *Nature Physics* **19**, 629 (2023).
- [55] Z. Dai, C. Lian, J. Lafuente-Bartolome, and F. Giustino, Excitonic Polarons and Self-Trapped Excitons from First-Principles Exciton-Phonon Couplings, *Phys. Rev. Lett.* **132**, 036902 (2024).
- [56] Z. Dai, C. Lian, J. Lafuente-Bartolome, and F. Giustino, Theory of Excitonic Polarons: From Models to First-Principles Calculations, *Phys. Rev. B* **109**, 045202 (2024).
- [57] F. S. Ham, Dynamical Jahn-Teller Effect in Paramagnetic Resonance Spectra: Orbital Reduction Factors and Partial Quenching of Spin-Orbit Interaction, *Phys. Rev.* **138**, A1727 (1965).
- [58] S. V. Streltsov and D. I. Khomskii, Jahn-Teller Effect and Spin-Orbit Coupling: Friends or Foes?, *Phys. Rev. X* **10**, 031043 (2020).
- [59] T. Lyu and P. Dorenbos, Bi^{3+} Acting Both as An Electron and as A Hole Trap in $\text{La-}, \text{Y-},$ and LuPO_4 , *Journal of Materials Chemistry C* **6**, 6240 (2018).
- [60] R. H. Awater, L. C. Niemeijer-Berghuijs, and P. Dorenbos, Luminescence and Charge Carrier Trapping in $\text{YPO}_4:\text{Bi}$, *Optical Materials* **66**, 351 (2017).
- [61] A. M. Srivastava and S. J. Camardello, Concentration Dependence of the Bi^{3+} Luminescence in LnPO_4 ($\text{Ln} = \text{Y}^{3+}, \text{Lu}^{3+}$), *Optical Materials* **39**, 130 (2015).
- [62] A. N. Trukhin and L. A. Boatner, Electronic Structure of ScPO_4 Single Crystals: Optical and Photoelectric Properties, *Materials Science Forum* **239-241**, 573 (1997).
- [63] A. H. Krumpel, A. J. J. Bos, A. Bessière, E. van der Kolk, and P. Dorenbos, Controlled Electron and Hole Trapping in $\text{YPO}_4 : \text{Ce}^{3+}, \text{Ln}^{3+}$ and $\text{LuPO}_4 : \text{Ce}^{3+}, \text{Ln}^{3+}$ ($\text{Ln} =$

Sm, Dy, Ho, Er, Tm), [Phys. Rev. B](#) **80**, 085103 (2009).
[64] A. J. J. Bos, P. Dorenbos, A. Bessière, and B. Viana,

Lanthanide Energy Levels in YPO_4 , [Radiation Measurements](#) **43**, 222 (2008).